Available online at www.sciencedirect.com

ScienceDirect

Procedia Engineering 133 (2015) 669 – 680

Procedia Engineering

www.elsevier.com/locate/procedia

6th Fatigue Design conference, Fatigue Design 2015

The Effect of Metal-Carbide Morphology on the Thermomechanical Fatigue (TMF) Behavior of Cast Austenitic Alloys for Exhaust Manifolds

Hailong Zhao[a,b], Carlos C. Engler-Pinto Jr.[b], Jacob Zindel[b], Larry Godlewski[b], Yinhui Zhang[a], Qiang Feng[a], Mei Li[b]*

[a]*National Center for Materials Service Safety, University of Science and Technology Beijing, Beijing 100083, China*
[b]*Ford Research and Advanced Engineering Laboratory, Dearborn 48124, USA*

Abstract

Out-of-phase thermomechanical fatigue (OP-TMF) tests between 600°C and 950°C have been conducted for three cast austenitic alloys with different metal-carbide (MC) morphologies: dense skeleton, sparse skeleton and blocky carbides. The alloy with dense skeleton-like MC exhibited longer TMF life than the other two, even though their chemical composition and casting process were similar. Fractography analysis indicated that the fatigue cracks initiated from the specimen surface for all the alloys in this study. The morphology of Nb(C,N) has an obvious effect on inelastic deformation. Alloys with skeleton-like Nb(C,N) precipitates have better ductility as compared to alloys with isolated blocky precipitates. Dense skeleton-like Nb(C,N) is found to delay OP-TMF crack initiation and propagation, resulting in longer TMF lives.

Peer-review under responsibility of CETIM

Keywords: thermomechanical fatigue; carbides morphology; austenitic cast steel

1. Introduction

Automotive exhaust manifolds, as the first components in the exhaust system connecting to the cylinder head, are subjected to cyclic thermal and mechanical loads due to restraints and thermal gradients arising during start-up, speed variation and shut-down operations. The thermomechanical fatigue (TMF) damage process in exhaust manifolds are primarily influenced by the exhaust temperature. Recently, exhaust regulations are becoming more stringent all over the world, resulting in continuously increasing exhaust temperature in modern gasoline cars [1,2]. Therefore, new materials, which can withstand higher temperature and have better TMF properties, are expected to

Peer-review under responsibility of CETIM
doi:10.1016/j.proeng.2015.12.648

be developed.

Austenitic cast steels are among the most suitable materials for gasoline exhaust manifolds due to their excellent resistance to oxidation, creep and high temperature fatigue [3]. To obtain complete austenite matrix and reduce the cost of new steels from expensive elements and post processing, the content of carbon and/or nitrogen have been increased to higher levels and no heat treatment is usually adopted. As a result, primary carbides and/or carbo-nitrides are precipitated inevitably at the interdendritic regions during solidification. Since no solution treatments is carried out, these primary precipitates are always present in the alloy [4]. Therefore, it is necessary to understand the mechanism by which these carbides and/or carbo-nitrides affect the TMF behaviour; this understanding is essential for new alloy design and TMF lifetime prediction.

Compared with wrought austenitic steels, very limited data is available for cast austenitic steels [5]. Published papers related to the fatigue behaviour of cast steels usually focus on the effect of carbide size [6]. In this paper, the effect of carbides morphology on TMF behaviour in austenitic cast steels is investigated.

2. Materials and Experimental Methods

2.1. Materials

To get different morphology of carbides, three alloys with two compositions and two casting processes (sand or metal molds) were generated. Their chemical compositions and corresponding casting process are indicated in Table 1. It can be seen that Alloys A and B have essentially the same composition, but different cooling rates during solidification; Alloy C is cast in sand molds but with different N and W contents. The as-cast microstructure of the three alloys is illustrated in Figure 1. Based on energy-dispersive x-ray spectroscopy (EDS) and x-ray diffraction (XRD) analysis results, Alloy A consists of dense skeleton-like Nb(C,N) (white phase in Figure 1a) in an austenite matrix. Compared with Alloy A, cooling rate of Alloy B during casting was higher, thus Nb(C,N) in Alloy B precipitated as sparse skeleton-like in an austenite matrix, as shown in Figure 1b. The morphology of Nb(C,N) in Alloy C is blocky or rod-like, as shown in Figure 1c, which is significantly different from the other two alloys.

Table 1. Chemical compositions and casting molds of the three alloys (wt.%).

Alloy Name	Casting Mold	Fe	Cr	Ni	Nb	C	Si	Mn	N	W
A	Sand	Bal.	20.0	10.2	2.0	0.31	0.9	1.1	0.16	-
B	Metal	Bal.	19.7	10.1	2.1	0.29	0.8	0.9	0.15	-
C	Sand	Bal.	21.8	9.4	2.4	0.54	1.1	1.1	0.32	1.2

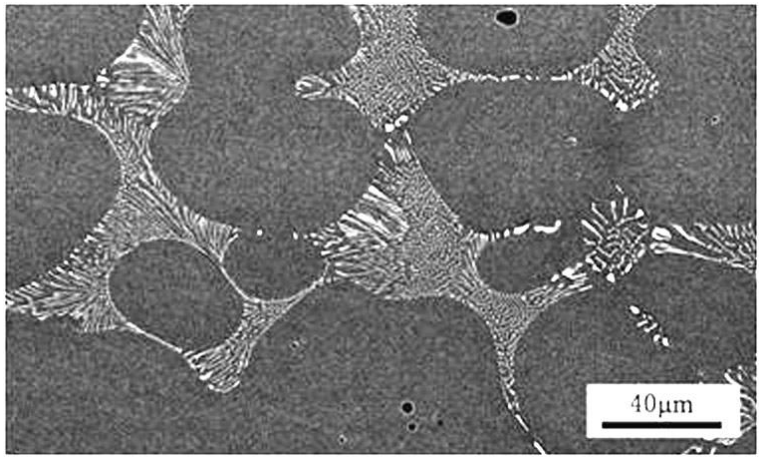

(a)

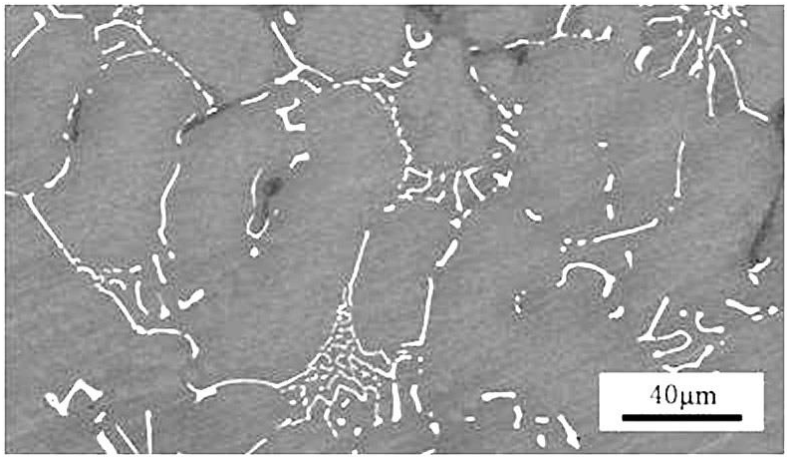

(b)

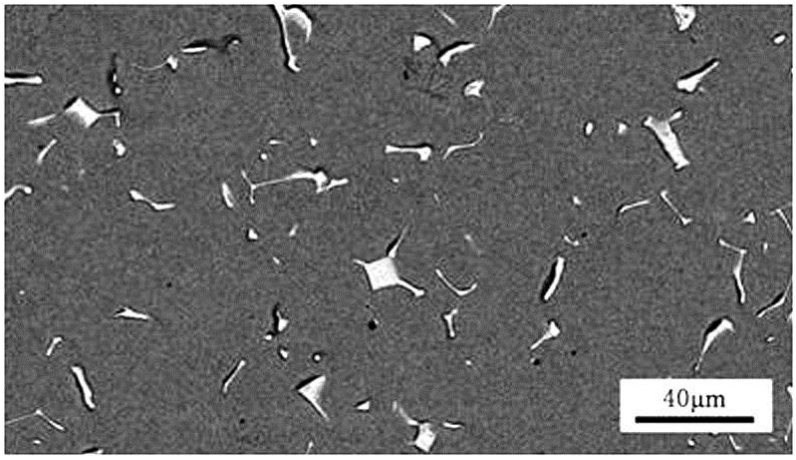

(c)

Fig. 1. As-cast microstructures of the investigated steels, observed by SEM with backscattered electron contrast: (a) Alloy A; (b) Alloy B; (c) Alloy C.

2.2. Experimental procedures

Tensile tests were carried out at room temperature. The specimens were dog-bone shape with the gauge diameter of 8.88 mm and the gauge length of 44.4 mm, in accordance with ASTM standard E8-2013. The tests were strain controlled and the strain rate was 0.5% per minute.

Out-of-phase thermomechanical fatigue tests were conducted in air under strain control in the temperature range of 600-950 °C using a servo-hydraulic fatigue testing machine with a high frequency inductive heating device. The strain feedback was provided by a high-temperature extensometer. During the tests, strain and temperature were directly PID controlled and followed a triangular shape wave. Ten thermal cycles without load were conducted between 600-950 °C prior TMF testing to acquire the thermal strain. The total strain to be controlled during the test is determined by the thermal strain plus the target mechanical strain. Three mechanical strain ranges were tested for all materials: 0.4%, 0.6% and 0.8%. Cylindrical TMF specimens with a gauge length of 22 mm and a diameter of 7.6 mm were used. The temperature gradient along the gauge area in the axial direction was checked with three thermocouples (Type K) attached at different locations within the gauge length and controlled to be below 1% of the maximum temperature. During testing, a two-color infrared pyrometer was employed to measure the temperature in the middle of gauge length and provide the feedback signal for the induction heater. The fatigue life was determined at the cycle where a 10% drop in the maximum stress was detected. Fractographic observations were carried out on scanning electron microscopy and optical stereo macroscopy.

3. Results and Discussion

3.1. Room temperature tensile tests

Figure 2 shows the strain-stress curves obtained at room temperature tensile testing for Alloy A, B and C. The yield strength of Alloy C is higher than Alloys A and B, while the ductility of Alloy C is much lower. Alloys A and B have very similar stress-strain behavior due to their similar composition and carbide morphology. It seems that the difference in lamellar spacing within Nb(C,N) does affect the deformation behavior at room temperature. According to data from the Hitachi patent US8241558 B2 [7], good ductility usually means good thermal fatigue resistance, so Alloys A and B should have better thermal fatigue resistance than Alloy C.

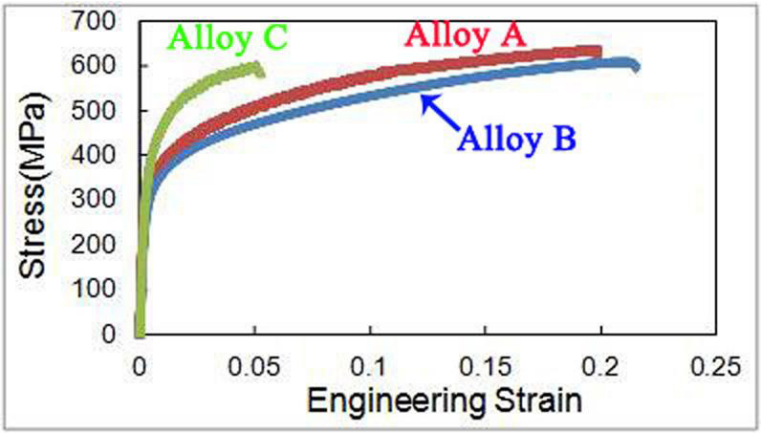

Fig. 2. Typical tensile curves for Alloys A, B and C at room temperature.

3.2. TMF life and stress-strain response

The TMF results of are shown in Figure 3. It can be observed that the fatigue life for Alloy A is remarkably

longer than the other two alloys at all the mechanical strain ranges. Even though the room temperature ductility of Alloys A and B are very similar, the TMF behaviour is very different. In fact, Alloy A, with dense skeleton-like Nb(C,N) has improved TMF resistance. As the main difference between Alloys A and B is the solidification rate, it seems that a fine Nb(C,N) lamellar spacing is preferred for TMF resistance (compare Figures 1a and 1b). A precise measurement of Nb(C,N) lamellar spacing has not been completed, but based on Figure 1, it can be estimated that the lamellar spacing for Alloy A is around 5 times smaller than that of Alloy B.

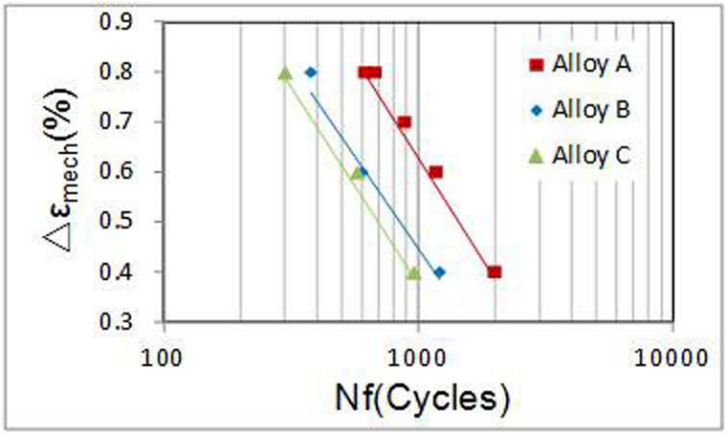

Fig. 3. Mechanical strain range versus cycles to failure in OP-TMF.

Figures 4a-c show the cyclic peak stress response at the strain ranges of 0.8%, 0.6% and 0.4%, respectively. It is clear that for the alloys investigated a higher tensile peak stress results in lower the TMF life. In OP-TMF, the maximum stress occurs at the lowest temperature of the cycle, where thermal recovery activities are relatively weak. Therefore, higher stress at low temperatures results in more severe local damage, which can explain the shorter fatigue life of Alloy C (highest peak stresses).

Figure 5 shows the hysteresis stress-strain curves at the mid-life cycle with different applied mechanical strain ranges. It can be seen that the maximum compressive stress doesn't occur at the minimum strain, due to the decrease in the material yield strength with temperature. The maximum tensile stress, however, always occur at the maximum mechanical strain, which corresponds to the minimum temperature of the TMF cycle. The width of the hysteresis loop at zero stress corresponds to the cyclic inelastic strain range [8]. Alloy C has a higher yield strength than Alloys A and B, so the peak stress achieved during a TMF cycle is higher; this indicates that dislocation motion is relatively more difficult in Alloy C and that the interaction forces between dislocations and barriers (precipitates) are stronger. Alloys A and B have similar cyclic deformation behaviour, probably due to the common morphology of Nb(C,N) carbides, although Alloy A is slightly softer than Alloy B. These relations are more clearly illustrated in Figure 6, which plots the TMF cyclic stress-strain behaviour at mid-life for all three alloys. Figure 7 shows the average modulus of elasticity as a function of temperature measured from room temperature to 950°C. It can be observed that the modulus of elasticity for all three alloys decreases approximately linearly with temperature. It is worthy to note that Alloy A has the lowest modulus and the best TMF performance.

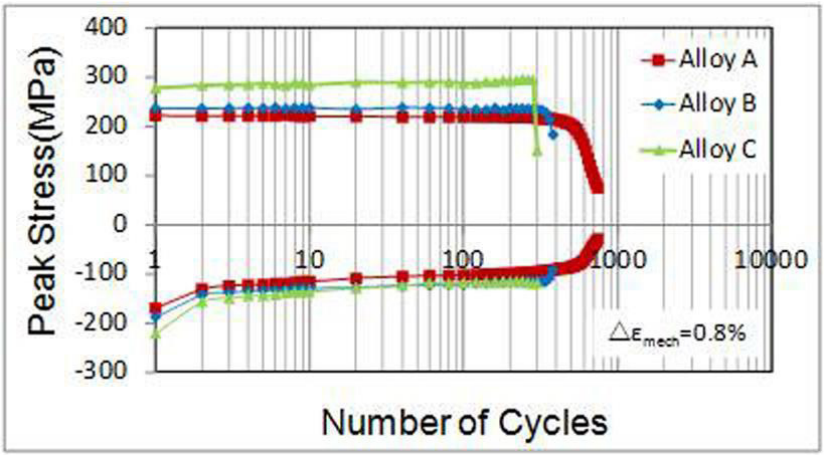

(a)

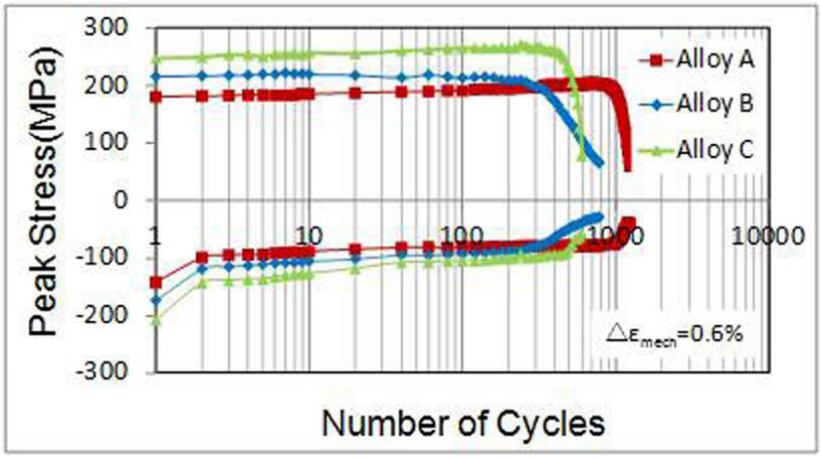

(b)

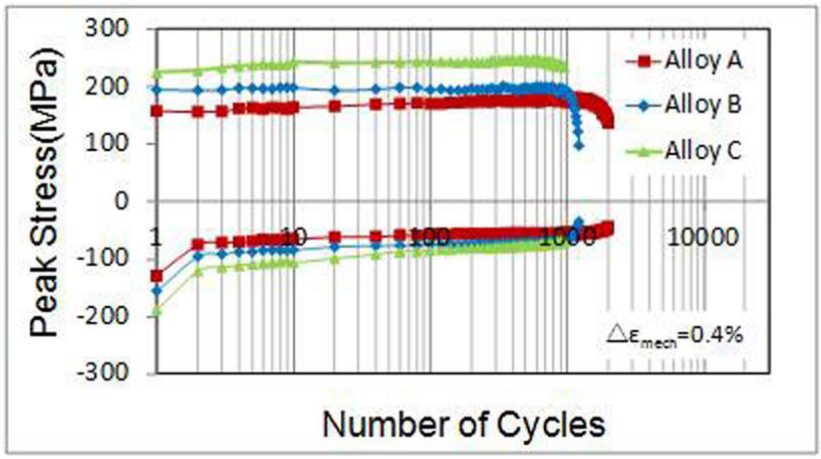

(c)

Fig. 4. Cyclic stress response curves at the mechanical strain ranges of (a) 0.8%, (b) 0.6%, and (c) 0.4% in OP-TMF.

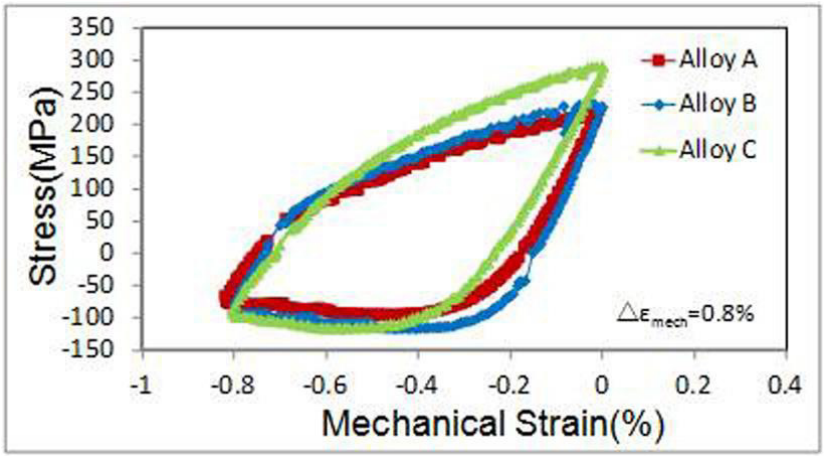

(a)

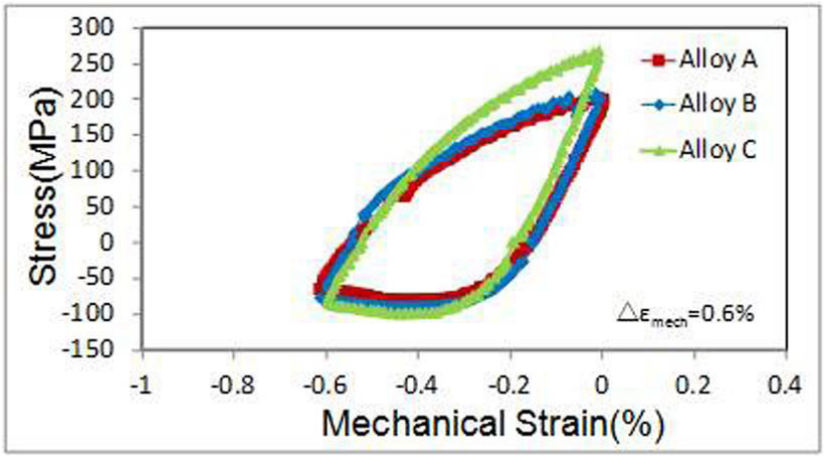

(b)

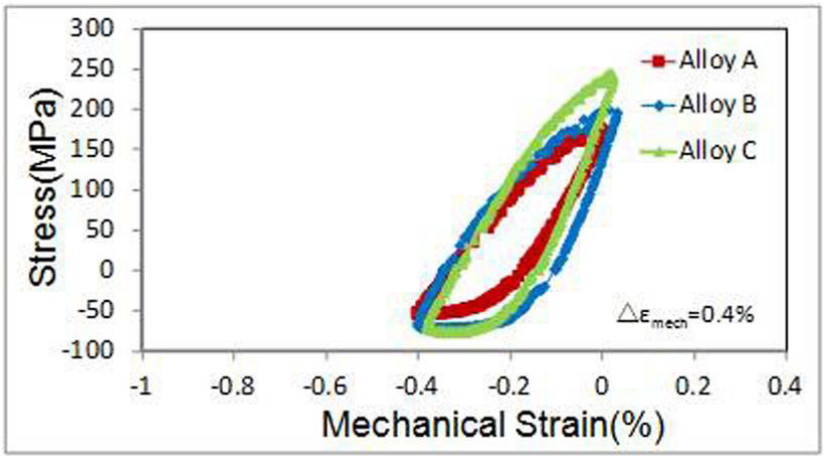

(c)

Fig. 5. Stress-strain hysteresis loops at mid-life cycles for mechanical strain ranges of (a) 0.8%, (b) 0.6%, and (c) 0.4% in OP-TMF.

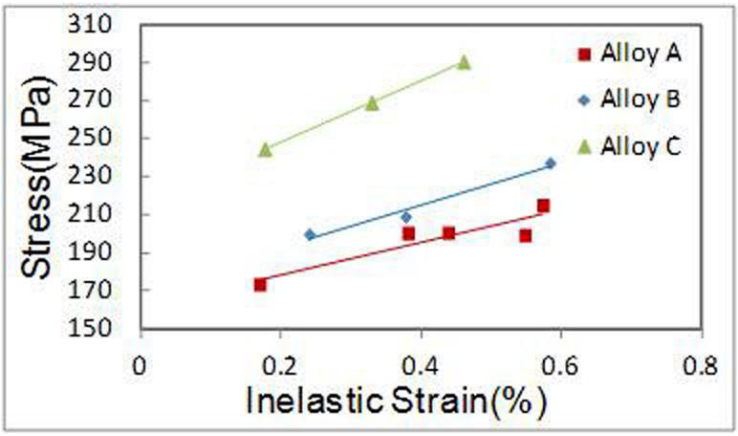

Fig. 6. Cyclic stress-strain behavior in OP-TMF.

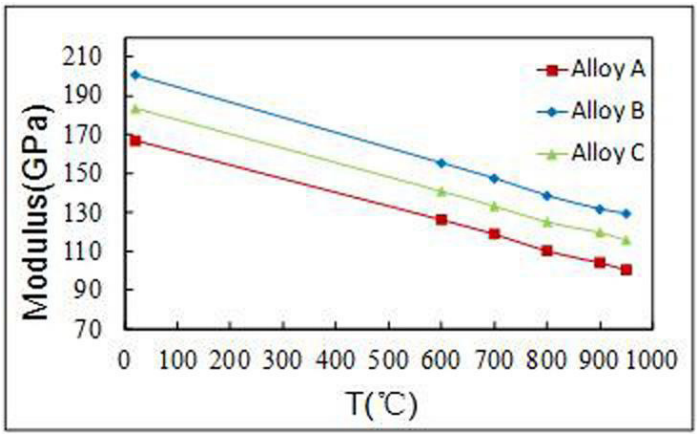

Fig. 7. Modulus of elasticity measured from room temperature to 950°C before TMF testing (average of all samples).

3.3. Fractography

The fracture surface for the sample from Alloy A tested under OP-TM at a strain range of 0.8% is shown in Figure 8. Figure 8(a) shows an overview of the entire fracture surface; a careful examination of the fracture surface under SEM and optical stereo macroscopy allows to distinguish three distinct areas within the fracture surface of the tested samples, as indicated in Figure 8(a): region I, corresponding to the crack initiation (and small crack propagation) region; region II, corresponding to the large fatigue crack propagation area, after the multiple cracks initiated in region I have merged; and region III, corresponding to the final fracture by tensile overload, when the remaining area within the section is too low to sustain the applied maximum load. Figure 8(b) shows a higher magnification view of region I, which is characterized by its flat appearance, perpendicular to the applied load, indicating that the crack propagation rate is relatively low in this region (the cracks propagate perpendicularly to the applied load, ignoring any microstructural features) . Ratchet-like features are seen around the surface in region I, indicating multiple crack initiation sites. Figure 8(c) illustrates the fracture appearance of region II, when the fatigue crack is large and propagates around microstructural features (dendrites), following a not-so-flat path; the surface in region II also show signs of oxidation. Finally, Figure 8(d) illustrates the final fracture by tensile overload, region II, where no oxidation is present, the fracture surface is rougher than regions I and II, and ductile dimples can be observed.

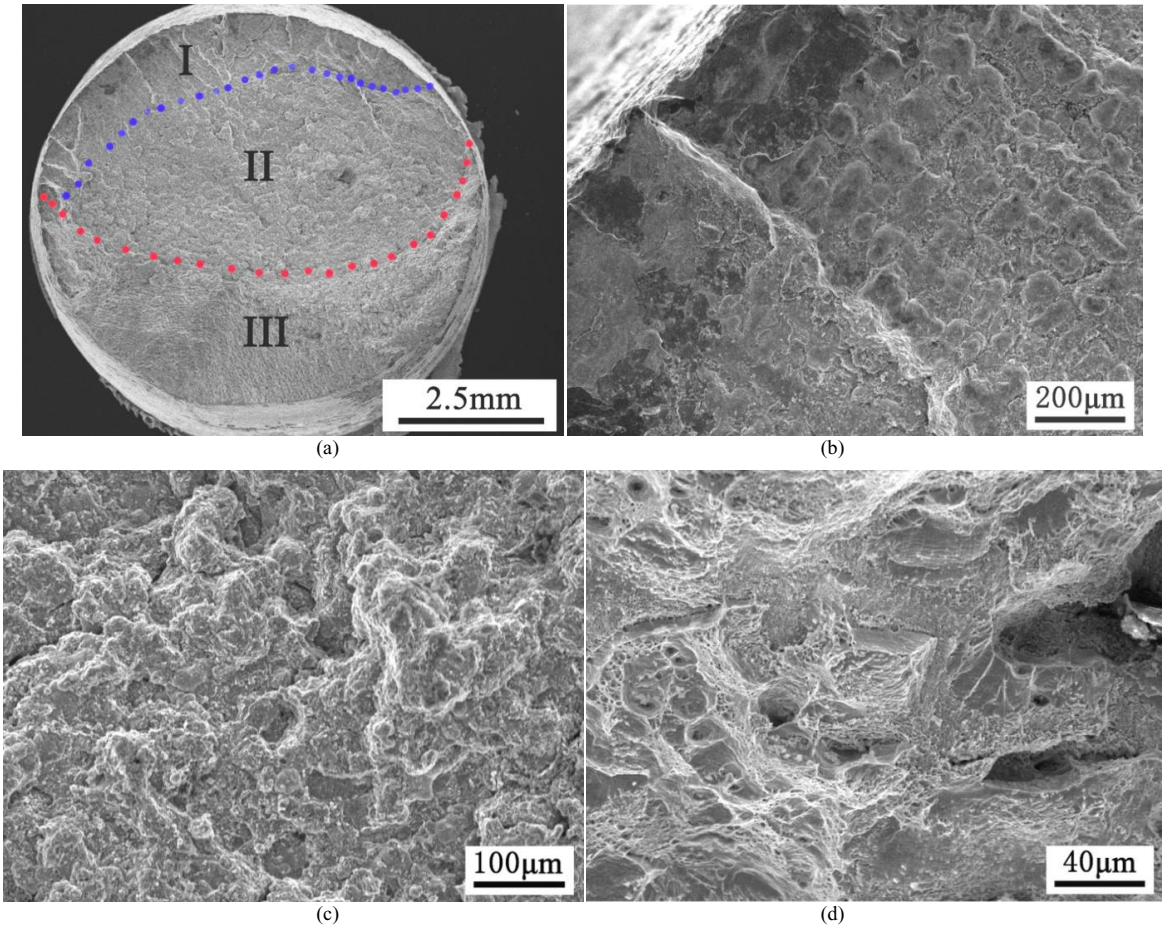

Fig. 8. Fracture surface of Alloy A at the mechanical strain range of 0.8%: (a) entire fracture surface displaying tree distinct areas; (b) magnified view of Region I; (c) magnified view of Region II; (d) magnified view of Region III.

The fractography study for the sample tested at 0.8% strain range from Alloy B is summarized in Figure 9. Similarly to Figure 8 (Alloy A), the fracture surface can also be divided in three regions: region I, crack initiation; region II, large crack propagation; and region II, final fracture – as illustrated in Figure 9(b)-(f). Cracks also initated from the sample surface, but a higher number of initiation sites are observed for Alloy B (as compared to Alloy A). All three regions observed in Alloy B present very similar features to the ones observed for Alloy A. Interestingly, a large casting defect (shrinkage pore, Figure 9f) was observed in the final fracture portion of this sample, but it does not seem to have influenced the fatigue life.

Figure 10 shows the fracture surface of the OP-TMF sample from Alloy C, also tested at the mechanical strain range of 0.8%. Compared with Alloys A and B, it was not so easy to distinguish regions I, II, and II for this alloy. It was in fact needed to combine the images taken by SEM in Figure 10(a) and by stereo macroscopy in Figure 10(b), to properly identify the three distinct regions. Overall, the fracture surface is relatively less flat (as compared to Alloys A and B), which indicates that the fatigue crack probably propagated faster, consistent with the observed lower fatigue life for this alloy. There seems to be a single main crack initiation site, also located at the sample surface.

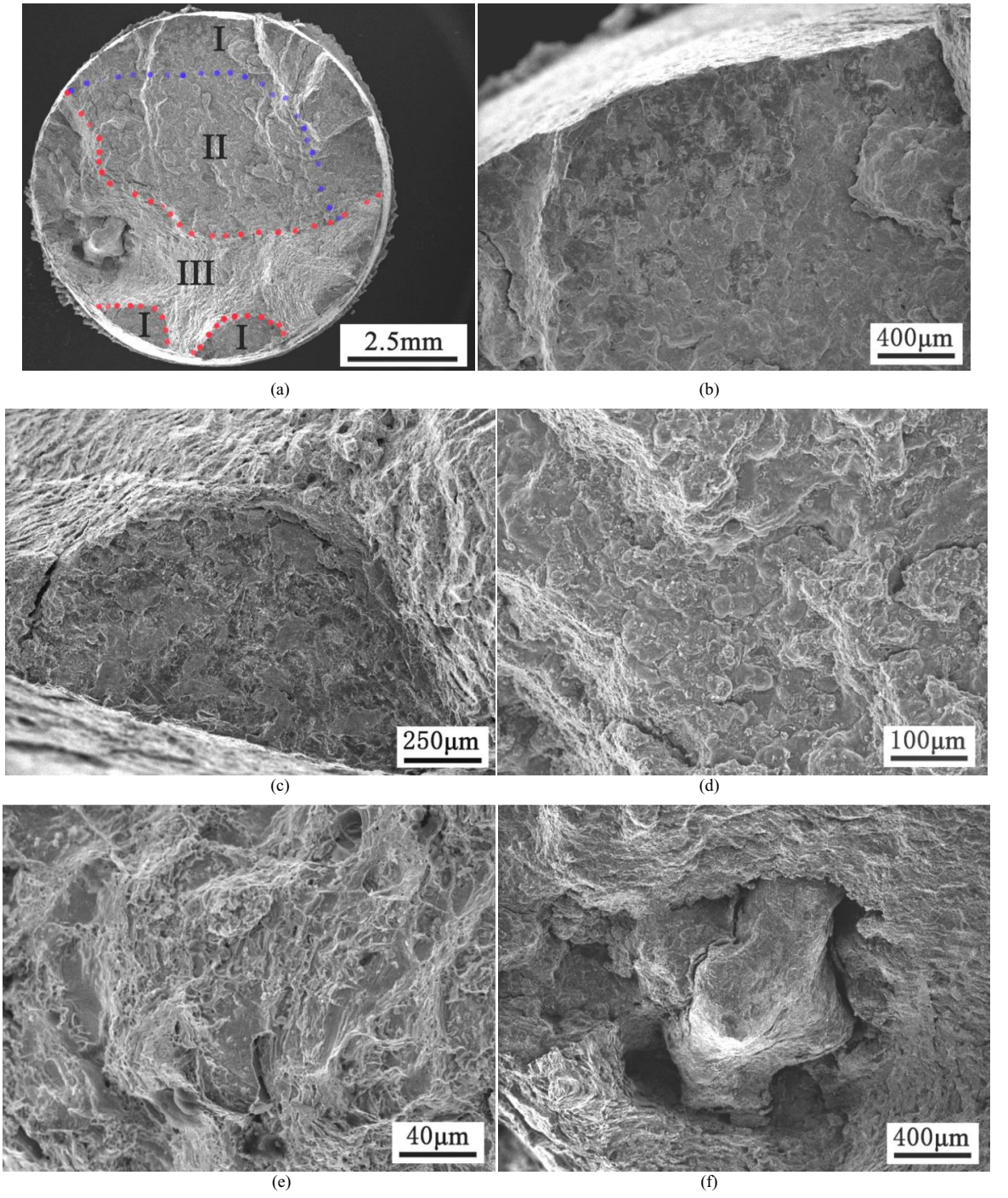

(a) (b)

(c) (d)

(e) (f)

Fig. 9. Fracture surface of Alloy B at the mechanical strain range of 0.8%: (a) entire fracture surface displaying tree distinct areas; (b) magnified view of Region I at the top; (c) magnified view of Region I at the bottom; (d) magnified view of Region II; (e) magnified view of Region III; (f) casting defect in Region III.

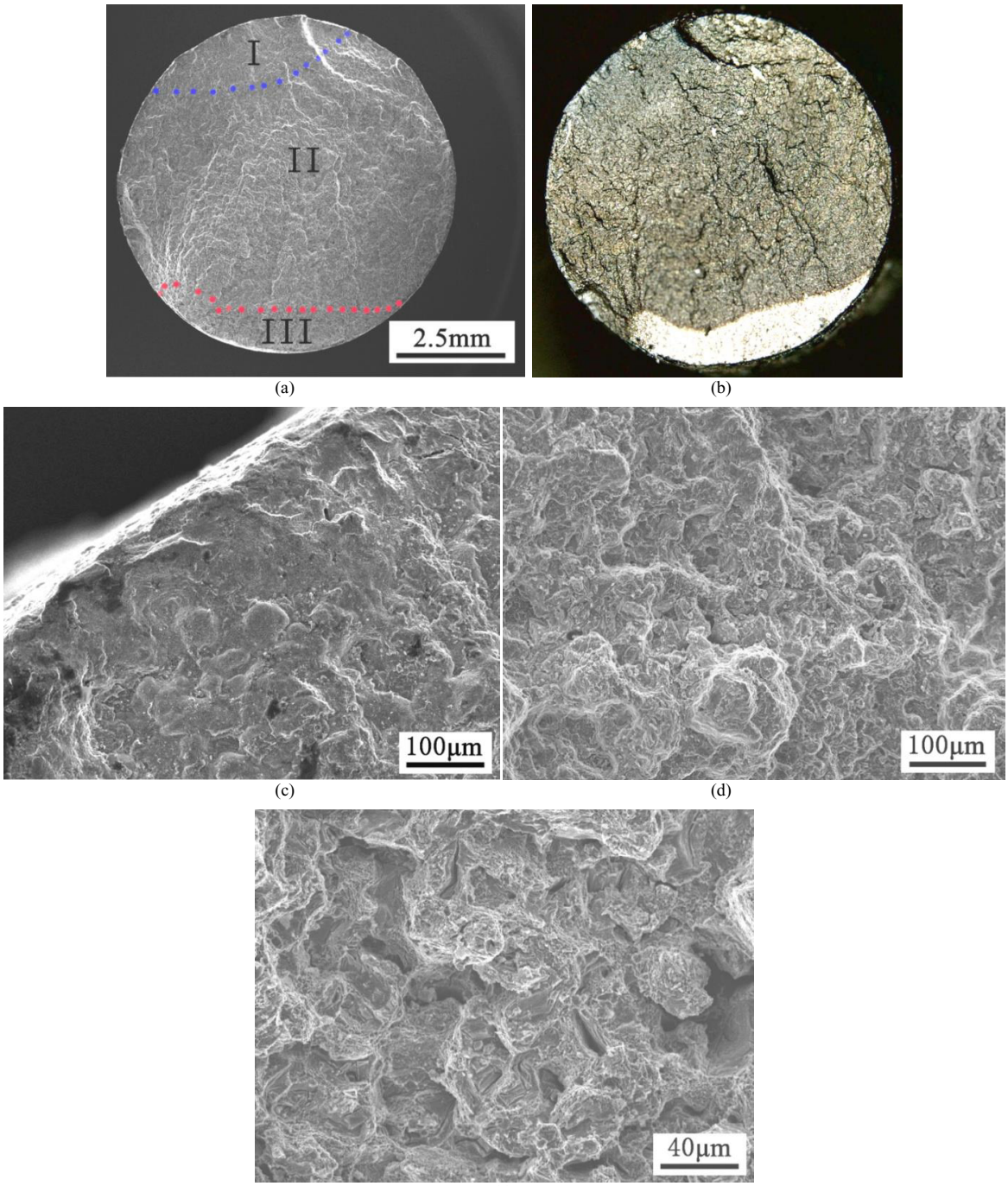

Fig. 10. Fracture surface of Alloy C at the mechanical strain range of 0.8%: (a) entire fracture surface displaying tree distinct areas (SEM); (b) entire fracture surface under optical microscopy; (c) magnified view of Region I; (d) magnified view of Region II; (e) magnified view of Region III.

4. Conclusions

Based on the OP-TMF test results of the three cast austenitic steels, the following conclusions can be drawn:

1) The morphology of Nb(C,N) has an obvious effect on inelastic deformation. Alloys with skeleton-like Nb(C,N) precipitates have better ductility as compared to alloys with isolated blocky precipitates.
2) Alloys with skeleton-like Nb(C,N) developed lower maximum stresses at all strain levels under OP-TMF loading.
3) Dense skeleton-like Nb(C,N) is found to delay OP-TMF crack initiation and propagation, resulting in longer TMF lives.

This study is still on-going. Longitudinal sections are currently being prepared to observe the effect of the microstructure on the crack propagation path. The results of this study will be object of a future publication.

Acknowledgements

This research is sponsored by University Research Program (URP) between Ford Motor Company and University of Science and Technology, Beijing. The author acknowledge financial support from China Scholarship Council. Special thanks to Prof. Simon Lekakh in University of Missouri Science and Technology for his help in alloy casting and Prof. Kai Sun in University of Michigan for his help in SEM training.

References

[1] A.Y. Karnik, M.H. Shelby, Effect of exhaust gas temperature limits on the peak power performance of a turbocharged gasoline engine, J. Eng. Gas Turb. Power 132 (2010) 112801–1–7.
[2] I.A. Sustaita Torres, S. Haro Rodríguez, M.P. Guerrero Mata, et al, Aging of a cast 35Cr-45Ni heat resistant alloy, Mater. Chem. Phys. 33 (2012) 1018–1023.
[3] I. Nikulin, A. Kipelova, R. Kaibyshev, Effect of high-temperature exposure on the mechanical properties of 18Cr-8Ni-W-Nb-V-N stainless steel, Mater. Sci. Eng., A 554 (2012) 61–66.
[4] M. Garbiaka, B. Piekarski, Phases in austenitic cast steel, Defect Diffus. Forum, 326-328 (2012) 215–220.
[5] Y.J. Kim, H. Jang, High temperature fatigue resistance of an ACI HH50-type cast austenitic stainless steel, Mater. Sci. Eng., A 527 (2010) 5415–5420.
[6] Y.J. Kim, H. Jang, Y.J. Oh, High temperature low cycle fatigue properties of a HF30-type cast austenitic stainless steel, Mater. Sci. Eng., A 526 (2009) 244–249.
[7] K. Hayashi, K. Itoh, A. Odaira, et al, High-Cr, high-Ni, heat-resistant, austenitic cast steel and exhaust equipment members formed thereby, US Patent: US8241558 B2, 2005.
[8] S.J. Ko, Y.J. Kim, High temperature fatigue behaviors of a cast ferritic stainless steel, Mater. Sci. Eng., A 534 (2012) 7–12.